ADVANCED ENGINEERING MATERIALS
www.aem-journal.com

Effect of Copper Content on the Microstructure and Mechanical Properties of As-Cast Refractory MoNbTi Multiprincipal Element Alloys

*Eder Lopes Ortiz, João Felipe Queiroz Rodrigues, Renato Baldan, Erik Poloni, Giovana da Silva Padilha, Wislei Riuper Osório, and Ausdinir Danilo Bortolozo**

Multiprincipal element alloys (MPEAs) exhibit a wide range of microstructures and mechanical properties, depending on composition and processing. In this study, the impact of Cu addition on the microstructure and mechanical performance of MoNbTi MPEAs is investigated. Cu plays a dual role, promoting the formation of strengthening intermetallic phases while, at higher concentrations, potentially increasing brittleness. It also influences diffusion kinetics and phase transformation, leading to dendritic refinement and the formation of Cu–Ti intermetallics. Phase diagram simulations predict the behavior of Cu_xMoNbTi alloys with varying Cu content ($x = 0$, 0.25, 0.5, 1.0, and 2.0). The alloys are synthesized by arc casting and analyzed using X-ray diffraction, scanning electron microscopy, and energy dispersive spectroscopy. Mechanical properties are evaluated through Vickers hardness and compressive testing. The results show that Cu enhances densification and refines the dendritic structure, increasing hardness and strength. However, excessive Cu content leads to an increased fraction of Cu-rich intermetallics. Hardness ranges from 515 ± 54 HV to 614 ± 47 HV, while UTS peaks at $\approx 2000 \pm 80$ MPa for $Cu_{0.5}$MoNbTi, nearly doubling that of MoNbTi. The well-distributed precipitate network in $Cu_{0.5}$MoNbTi enables effective plastic deformation by reducing stress concentrations and delaying crack formation. Cu tailors MPEA microstructures, optimizing properties for applications.

1. Introduction

Enhancing the mechanical, thermal, and chemical properties of materials is crucial to advancing modern engineering and technology.[1] Multiprincipal element alloys (MPEAs) have gained significant interest due to their potential to outperform traditional alloys in versatility and performance. Their compositional flexibility enables a wide spectrum of microstructures and properties, making them promising for high-performance applications.[2,3] However, synthesizing single-phase alloys high entropy as initially envisaged remains challenging.[4] While the increase in configurational entropy indicates the potential formation of solid solutions comprising many primary elements, experimental observations often reveal the presence of multiple phases rather than a single homogenous one.[5] This complexity is attributed to intricate atomic interactions and the need for precise control over synthesis and processing conditions.[6] Despite these challenges, research on MPEAs remains highly productive, continuously expanding the possibilities for designing materials with novel physical and mechanical properties.[1,4–8]

Within the field of MPEAs, combinations of molybdenum (Mo), niobium (Nb), and titanium (Ti) have gained attention for their remarkable properties.[9] Mo provides a high melting point, thermal conductivity, and resistance to wear and corrosion.[10] Nb enhances toughness and superconductivity, while Ti is valued for its low density, high strength-to-weight ratio, and biocompatibility.[11] Combination of

E. L. Ortiz, J. F. Queiroz Rodrigues, G. da Silva Padilha, W. R. Osório, A. D. Bortolozo
Centro de Pesquisa de Manufatura de Materiais Avançados - CPMMA
Faculdade de Ciências Aplicadas
Universidade Estadual de Campinas (Unicamp)
Rua Pedro Zaccarias, 1300, Limeira, SP 13483-350, Brazil
E-mail: ausdinir@unicamp.br

The ORCID identification number(s) for the author(s) of this article can be found under https://doi.org/10.1002/adem.202500866.

DOI: 10.1002/adem.202500866

E. L. Ortiz, J. F. Queiroz Rodrigues, W. R. Osório, A. D. Bortolozo
Faculdade de Tecnologia
Universidade Estadual de Campinas (Unicamp)
Paschoal Marmo, 1888, Limeira, SP 13484-332, Brazil

R. Baldan
Institute for Science and Engineering
São Paulo State University (UNESP)
Rua Geraldo Alckmin, 519, Itapeva, SP 18409-010, Brazil

E. Poloni
Centre for Advanced Structural Ceramics
Department of Materials
Imperial College London
London SW7 2AZ, UK

these elements can yield alloys with an optimal balance of strength, ductility, thermal stability, and corrosion resistance.[9,12,13] Chen and Li[14] demonstrated that selective laser melting of Nb, Mo, and Ti powders produces NbMoTi alloys with a dual-phase structure (BCC and face-centered cubic [FCC]), significantly improving hardness compared to pure metals.[14] Almeida et al. found that Ti–12Mo–13Nb and Ti–10Mo–20Nb alloys exhibit enhanced corrosion resistance and hardness-to-elasticity modulus ratios, particularly for biomedical implants, due to higher Nb content and reduced α-phase volume.[10] Kalali et al. showed that the addition of Ti refines grain size and increases hardness through solid solution hardening, making MoNbTi alloys suitable for applications requiring high specific strength.[15] Cieślak et al. studied high entropy alloys (HEAs) belonging to the Al–Ti–Mo–Nb–V system and identified a composition that exhibits strong ductility at low temperatures and corrosion resistance at high temperatures.[16] In these alloys, aluminum (Al) was essential for stabilizing the B2 phase and generating both the Mo-rich A15 phase and the Ti-rich secondary B2 phase.[16]

The incorporation of copper (Cu) into MPEA has been shown to improve mechanical properties and corrosion resistance.[17–23] Recent work indicates that the inclusion of Cu can promote the development of FCC phases, improving ductility and toughness in the alloys.[17] Cu also contributes to grain refinement and the formation of Cu-rich precipitates. These precipitates act as solid lubricants, increasing wear resistance at elevated temperatures.[17,18] Additionally, Cu plays a crucial role in forming compact, durable protective layers, such as chromium oxide (Cr_2O_3), which greatly enhances corrosion resistance in harsh environments such as sodium chloride (NaCl) solutions.[18] Passive films protect the alloys from localized corrosion and pitting, particularly in interdendritic zones where Cu segregation may occur. Cu has also been found to reduce the rate of corrosion and repel marine organisms, preventing their attachment.[18] The inclusion of Cu not only enhances the structural integrity and malleability of HEAs but also extends their longevity and resistance to corrosion, thereby justifying its use in demanding industrial environments and corrosive surroundings.[23] Despite these advantages, the addition of Cu to NbMoTi-based MPEAs remains unexplored, presenting a gap for further research.

The aim of this study is to investigate how Cu addition affects phase formation, microstructure, and mechanical properties in NbMoTi MPEAs. Specifically, we focus on the stabilization of selected phases and the development of precipitates. This work also explores how microstructural changes influence the hardness, yield strength, and ductility of the alloys.

2. Results and Discussions

2.1. Phase Diagram Simulations

Figure 1 illustrates the equilibrium phase diagrams obtained for the Cu_xMoNbTi alloys ($x = 0.25$, 0.5, 1.0, and 2.0), showing phase fractions as the system cools. Across all compositions, the solidification begins with the formation of a body-centered cubic (BCC) (B2) phase at 2200–2400 °C and proceeds through a sequence of phase transformations involving Cu–Ti intermetallics as the temperature decreases. The temperature ranges and the resulting phase fractions vary with copper content.

For the $Cu_{0.25}$MoNbTi and $Cu_{0.5}$MoNbTi alloys (Figure 1a,b), solidification starts with the BCC (B2) phase, followed by the formation of Cu_4Ti_3 ($x = 0.25$) or Cu_3Ti_2 ($x = 0.5$) at 950 °C and 870 °C, respectively. At temperatures below 750 °C, the γ-CuTi (B11) phase forms at different volume fractions, and by 200 °C, the BCC (B2) phase coexists with the $MoSi_2$ (C11b) prototype phase in both alloys. As copper content further increases ($x = 1.0$ and 2.0, Figure 1c,d), the solidification temperature of the BCC (B2) phase decreases (2170 °C for $x = 2.0$), and the residual liquid phase persists over a broader range. The Cu–Ti intermetallics transition from Cu_4Ti and Cu_3Ti_2 to Cu_4Ti_3 and γ-CuTi (B11) at lower temperatures during cooling. Below 200 °C, γ-CuTi (B11) remains in equilibrium with BCC (B2), with fractions of 0.47 and 0.53, respectively, for $x = 1.0$. For Cu_2MoNbTi, the increased Cu content reduces the total number of intermetallics formed but increases the fraction of Cu-rich phases, such as Cu_4Ti, which stabilizes at a higher fraction.

These findings reveal that increasing the Cu content lowers the solidification temperature of the BCC (B2) phase, decreases the number and increases the fraction of Cu-rich intermetallics formed, and shifts the equilibrium phase fractions toward Cu–Ti phases.

To better understand the solidification pathways of the Cu_xMoNbTi alloys, thermodynamic simulations were conducted using the Scheil model (**Figure 2**). For the $Cu_{0.25}$MoNbTi alloy, solidification initiates with the primary formation of a BCC (B2) phase, followed by minor formation of Cu–Ti intermetallics (Cu_4Ti_3, Cu_4Ti, Cu_2Ti) only in the final stages. The extended solidification range and limited segregation suggest that this composition favors a more homogeneous microstructure with low risk of embrittlement. In the $Cu_{0.5}$MoNbTi alloy, BCC (B2) remains the primary phase, but intermetallic compounds such as Cu_2Ti and Cu_4Ti_3 begin to form at higher volume fractions and earlier stages in the solidification sequence. Despite this, the balance between matrix and secondary phases remains favorable, allowing for the coexistence of strengthening mechanisms and acceptable ductility. As Cu content increases, the simulations indicate a marked shift toward the early and abundant formation of Cu-rich intermetallics. In the $Cu_{2.0}$MoNbTi composition, the solidification interval narrows significantly, and the residual liquid becomes highly enriched in Cu, resulting in extensive segregation and the predominance of brittle phases. Under equilibrium conditions, solidification occurs with the sequential formation of BCC (B2), Cu_4Ti_3, Cu_2Ti, and CuTi phases at temperatures relatively close to continuous solidification. In contrast, under the Scheil model, early separation of Cu- and Ti-rich phases occurs at very low solid fractions, intensifying the tendency for interdendritic segregation. This divergence confirms the expectation that Cu is rapidly rejected from the dendrite core, accumulating in interdendritic regions and forming intermetallics phases than predicted under equilibrium conditions.

Figure 3a presents the X-ray diffraction (XRD) patterns of the as-cast alloys, showcasing the evolution of phases with varying copper content. Across all compositions, the primary phase is BCC, with lattice parameters shifting systematically as Cu is introduced. In MoNbTi, the BCC phase exhibits a lattice

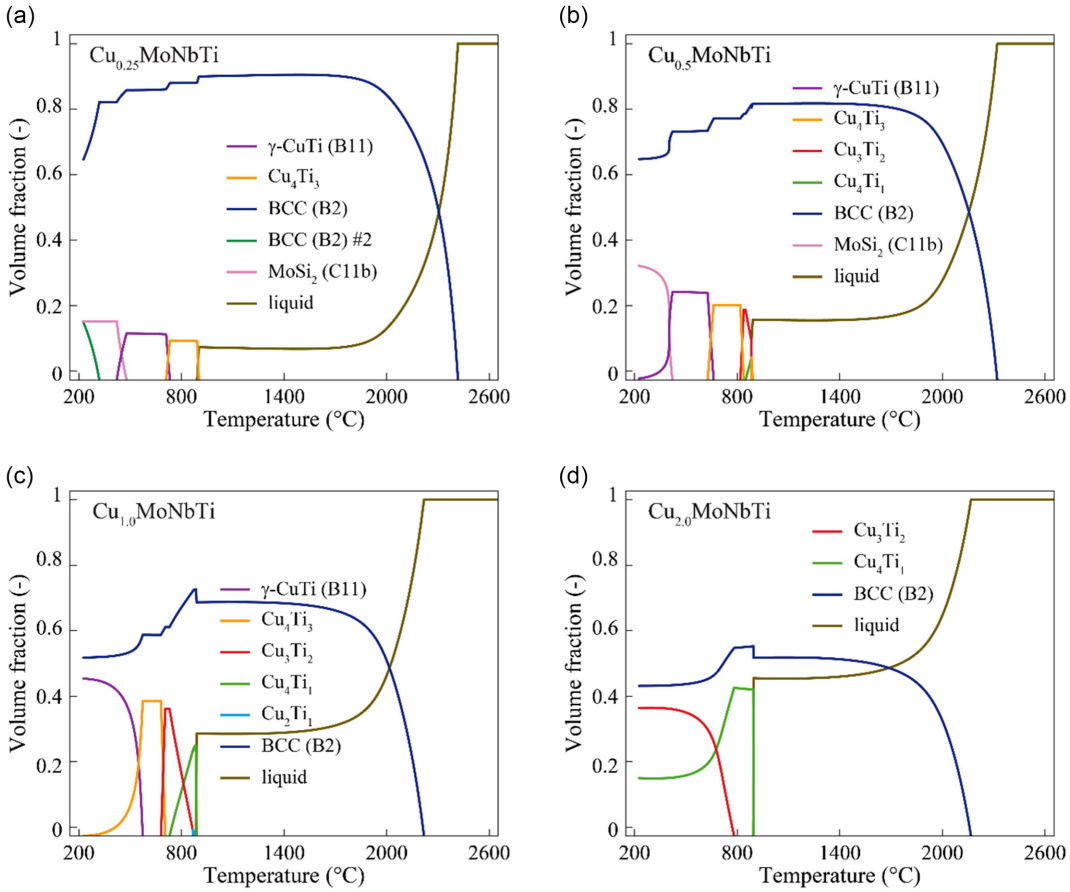

Figure 1. Phase diagram simulations for Cu_xMoNbTi alloys: a) $x = 0.25$, b) $x = 0.5$, c) $x = 1.0$, and d) $x = 2.0$.

parameter of 3.23 Å. Titanium enhances the thermodynamic stability of the MoNbTi alloy by refining the grain structure and increasing lattice distortion, which strengthens the solid solution and stabilizes the BCC phase at high temperatures.[15] As Cu is added to the alloys, subtle lattice distortions are observed in the solid solution phase, evidenced by the gradual reduction in lattice parameter shown in Figure 3b. Values of 3.230, 3.215, 3.210, 3.208, and 3.205 Å were found for the lattice parameter of Cu_xMoNbTi alloys with $x = 0$, 0.25, 0.5, 1.0, and 2.0, respectively. These distortions correlate with the selective interaction between Cu and Ti, promoting the formation of Cu–Ti intermetallic compounds.

Simulations and expanded baseline analysis of the diffractograms suggest the emergence of a Cu_3Ti_2 intermetallic phase even at low Cu content. At higher Cu contents, the formation of the Cu–Ti intermetallic phases Cu_4Ti and Cu_4Ti_3 becomes pronounced. The relatively weak diffraction signal from these phases suggests that they likely segregate into interdendritic regions. The increasing prevalence of intermetallic compounds with higher Cu content is accompanied by further shifts in the BCC lattice planes, indicating Ti depletion from the solid solution. This trend reflects the strong chemical affinity between Cu and Ti, in contrast to the Ti–Mo and Ti–Nb systems, which do not form intermetallics despite their miscibility.

2.2. Microstructural Characterization

Figure 4 shows SEM images of the Cu_xMoNbTi alloys taken with a backscattered electron detector. The images, combined with EDS point analysis, reveal significant morphological changes caused by Cu addition, which can be attributed to solidification mechanisms and fluid dynamics governing microstructural formation in metallic systems. During solidification, dendrite formation arises from the interplay between thermal gradients, solute redistribution, and crystallographic growth. Segregation not only promotes the formation of dendrites but also of intermetallic phases, influencing the overall microstructure. In the Cu_xMoNbTi alloys, the high partition coefficient of Cu leads to its segregation, enhancing concentration gradients in the liquid phase and driving the development of intricate dendritic structures.[24,25] Similarly, regions of Ti segregation are found to be surrounded by intermetallic compounds, reflecting the complex interactions among elements during solidification.

The trends observed in these alloys highlight the dual role of Cu. On the one hand, Cu promotes the formation of intermetallic phases, which act as barriers to dislocation motion. This precipitation hardening effect increases hardness and strength. On the other hand, excessive intermetallic formation reduces the system's mixing entropy, potentially compromising thermal

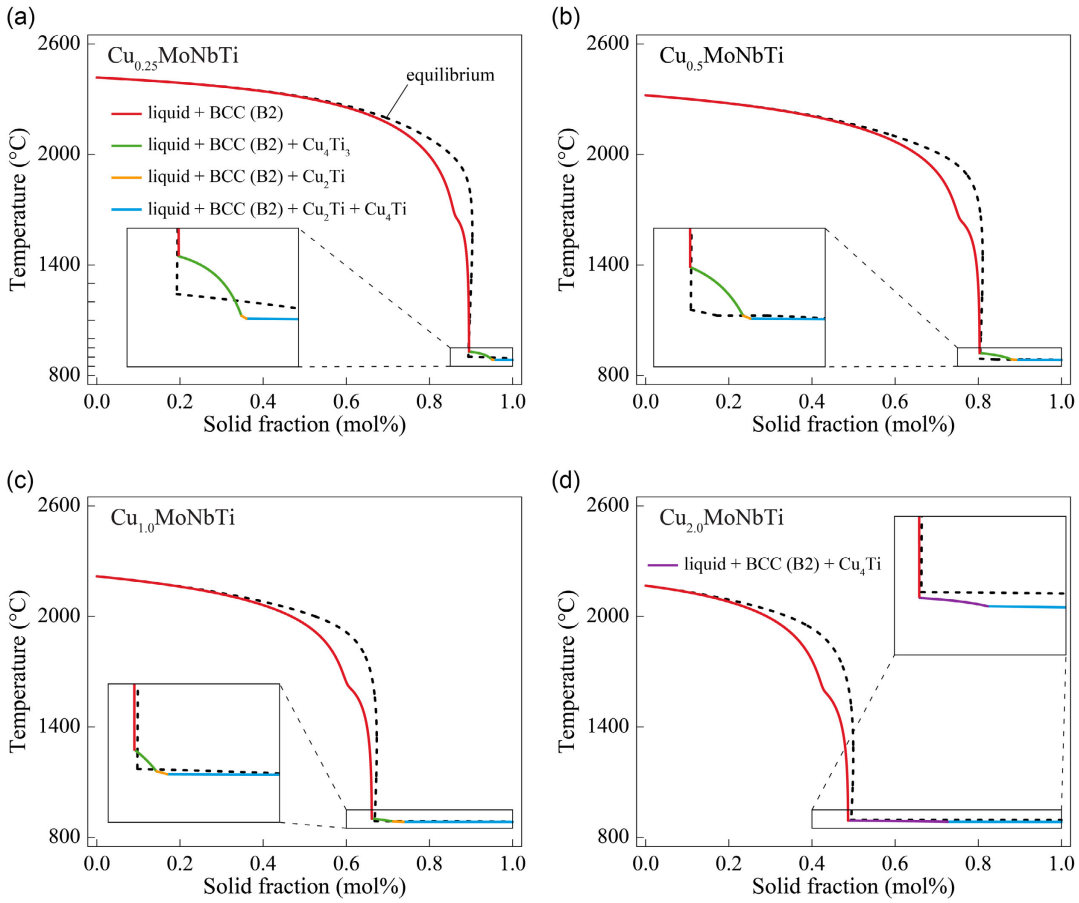

Figure 2. Scheil–Gulliver solidification simulations of $Cu_xMoNbTi$ alloys showing the evolution of phase formation as a function of solid fraction under nonequilibrium conditions: a) $x = 0.25$, b) $x = 0.5$, c) $x = 1.0$, and d) $x = 2.0$. [Correction added on 4 September 2025, after first online publication: Figure 2 has been updated in this version.]

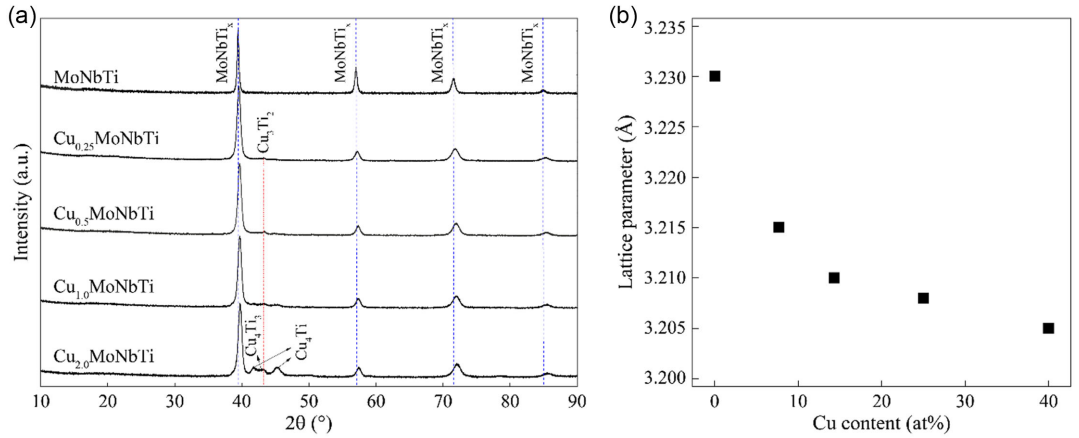

Figure 3. a) X-ray diffractograms of the $Cu_xMoNbTi$ alloys evidencing the presence of intermetallic compounds. b) Lattice parameter of the solid solution phase. $Cu_xMoNbTi$ alloys with $x = 0$, 0.25, 0.5, 1.0, and 2.0 correspond to Cu contents of 0, 7.7, 14.3, 25, and 40 at%, respectively.

stability and increasing brittleness. Achieving an ideal intermetallic fraction is crucial for balancing mechanical performance and entropy-driven stability, a key consideration for MPEAs.

As described by Li et al.[26] and Aguilar et al.,[27] the positive mixing enthalpy between Cu and Nb, as well as between Cu and Mo, indicates a low chemical affinity between these element pairs. This significantly contributes to the interdendritic

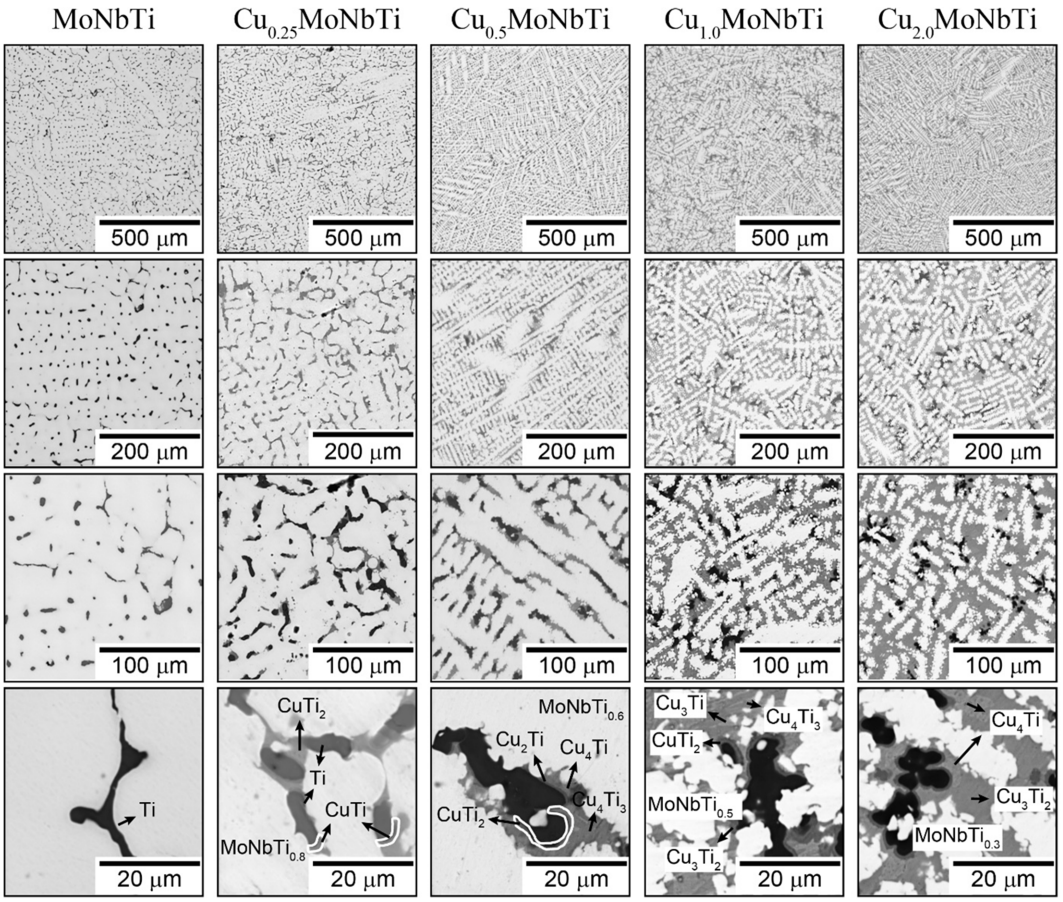

Figure 4. Scanning electron micrographs of the Cu_xMoNbTi alloys at different magnifications.

segregation of Cu during solidification, especially under rapid cooling conditions, as observed in arc-melted alloys. This behavior was documented, for instance, by Xian et al.,[21] who reported significant Cu segregation in CrMnFeCoNiCu_x alloys, forming Cu- and Mn-enriched interdendritic regions. In the present work, this segregation was confirmed by SEM and EDS and is consistent with thermodynamic data suggesting low solid solubility of Cu in BCC matrices rich in Mo and Nb. This segregation creates a local environment favorable to the formation of secondary phases. The strong affinity between Cu and Ti, reflected in the negative formation enthalpies of compounds such as Cu–Ti, results in the spontaneous precipitation of intermetallics in Cu- and Ti-rich regions. Studies such as Liu et al.[28] also show that Cu-enriched zones can promote preferential dissolution and thus influence both corrosion resistance and mechanical strength in those regions. This combination of segregation driven by positive mixing enthalpy and precipitation driven by local negative formation enthalpy constitutes an effective mechanism for strengthening via intermetallic phases but can also lead to a transition from ductile to brittle behavior, especially when such intermetallics are distributed in a discontinuous or uncoordinated manner.

In arc-melted alloys, the combination of high thermal gradients and rapid cooling rates leads to nonequilibrium solidification, enhancing solute segregation phenomena. The positive mixing enthalpy between Cu and refractory elements such as Mo and Nb limits Cu solubility in the solid BCC phase, promoting its rejection into the liquid during solidification. As solidification progresses, this partitioning effect concentrates Cu in the interdendritic liquid, amplifying constitutional undercooling ahead of the solidification front. This enhanced undercooling, combined with the reduced local melting point in Cu-enriched regions, increases the nucleation rate of secondary phases and restricts the growth of dendrites. As a result, finer dendritic structures are formed, particularly in alloys with moderate Cu content. Moreover, the strong chemical affinity between Cu and Ti, associated with negative formation enthalpies, further promotes the precipitation of intermetallic compounds, which may nucleate within interdendritic channels or near the dendrite arms, modifying the local solidification front and accelerating morphological refinement.

Figure 5 presents the EDS elemental mapping of the CuxMoNbTi alloys, revealing elemental segregation, particularly of Cu, within interdendritic regions. This observation aligns with the thermodynamic predictions and supports the formation of compositionally distinct microstructural domains, despite the general phase identification by XRD shown in Figure 3.

Segregation, a common phenomenon during alloy solidification, occurs due to differences in element solubility between the

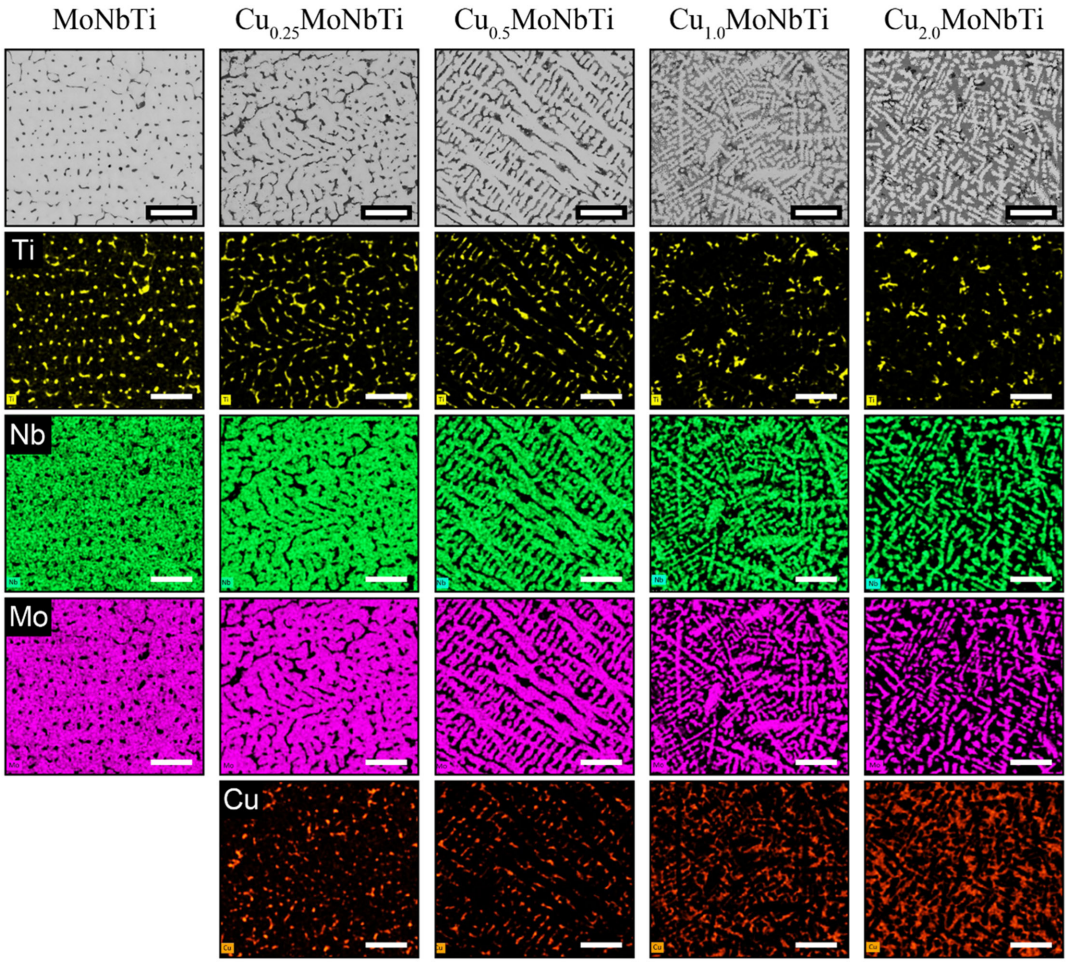

Figure 5. Elemental distribution of the as-cast Cu_xMoNbTi alloys. The first row displays backscattered electron images, providing compositional contrast. The subsequent rows display the spatial distribution of elements through EDS elemental maps for Ti, Nb, Mo, and Cu. Scale bars: 80 μm.

solid and liquid phases, leading to partitioning. Elements with low partition coefficients ($k < 1$) are pushed into the liquid phase, causing microsegregation within dendritic arms and macrosegregation throughout the casting.[24,29] Understanding this process requires insight into nucleation and growth mechanisms during cooling, which dictate the distribution of alloying elements.[24,25] EDS point analysis (Figure 4) and elemental mapping (Figure 5) were used to identify the phases formed upon solidification and verify their distribution within the as-cast alloys. **Table 1** compares the phases predicted by thermodynamic simulations with those identified using EDS in the Cu_xMoNbTi samples.

The overall elemental composition of the MoNbTi alloy closely matches its nominal proportions, and its homogeneous microstructure indicates effective solidification during casting. The solid solution matrix (MoNbTi) features equiaxed grains dominated by Mo and Nb. A slight tendency toward dendritic formation is observed, with Ti-rich regions segregated within interdendritic zones, resulting in a dendritic spacing of ≈42.3 (±1.5) μm. This aligns with the MoNb phase diagram, which indicates complete miscibility.[30]

As Cu is added to the alloys, significant microstructural changes occur. The $Cu_{0.25}$MoNbTi alloy exhibits a reduction in secondary dendrite arm spacing (λ_2) from ≈42.3 (±1.5) μm to ≈19.0 (±2.0) μm. EDS confirms the presence of CuTi and $CuTi_2$, but Cu_4Ti_3 was not detected. In $Cu_{0.5}$MoNbTi, EDS reveals the presence of Cu_4Ti_3, Cu_3Ti_2, Cu_4Ti, and Cu_2Ti. The λ_2 decreases further to ≈15.4 (±1.5) μm, with tertiary arm spacings (λ_3) of ≈3.4 (±0.4) μm. $Cu_{1.0}$MoNbTi contains Cu_4Ti_3, Cu_3Ti_2, Cu_3Ti, and $CuTi_2$, with intermetallics forming in larger interdendritic regions as Cu content increases. In $Cu_{2.0}$MoNbTi, λ_2 remains constant at 12.5 (±2) μm, with λ_3 slightly decreasing to 3.0 (±0.5) μm. Cu_3Ti_2

Table 1. Comparison of the phases predicted by thermodynamic simulations (Figure 1) with those identified using energy dispersive spectroscopy (EDS, Figure 3) in the Cu_xMoNbTi samples ($x = 0$, 0.25, 0.5, 1.0, and 2.0).

Cu content [at%]	Predicted	Detected by EDS
7.7	CuTi, Cu_4Ti_3, $CuTi_2$ ($MoSi_2$ prototype)	CuTi, $CuTi_2$
14.3	CuTi, Cu_4Ti_3, Cu_3Ti_2, Cu_4Ti, $CuTi_2$ ($MoSi_2$ prototype)	Cu_4Ti_3, Cu_3Ti_2, Cu_4Ti, Cu_2Ti, $CuTi_2$
25	CuTi, Cu_4Ti_3, Cu_3Ti_2, Cu_2Ti, Cu_4Ti	Cu_4Ti_3, Cu_3Ti_2, Cu_3Ti, $CuTi_2$
40	Cu_3Ti_2, Cu_4Ti	Cu_3Ti_2, Cu_4Ti

and Cu_4Ti form a rosette-like morphology in interdendritic regions. Similar features are observed in $Cu_{1.0}$MoNbTi and $Cu_{0.5}$MoNbTi, but they are less pronounced due to lower Cu content.

Overall, the microstructural evolution shows progressive dendritic refinement and the formation of Cu–Ti intermetallics with increasing Cu content, in agreement with thermodynamic simulations (Table 1). However, some discrepancies exist between simulated and experimentally detected phases. While Cu_4Ti_3 was predicted for $Cu_{0.25}$MoNbTi, it was not observed, and Cu_2Ti was found in $Cu_{0.5}$MoNbTi instead of CuTi. Additionally, some phases predicted at 200 °C, such as CuTi for $Cu_{0.25}$MoNbTi, were absent in the as-cast microstructure, likely due to phase evolution during cooling. In contrast, most phases expected to persist at lower temperatures ($CuTi_2$ for both $Cu_{0.25}$MoNbTi and $Cu_{0.5}$MoNbTi, and Cu_3Ti_2 and Cu_4Ti for $Cu_{2.0}$MoNbTi) showed good agreement with EDS. The discrepancies observed between the phase predictions and the experimental results can be attributed to multiple interrelated factors. The prediction tools used in this work rely on thermodynamic equilibrium conditions. Because solidification occurs under significant thermal gradients and high cooling rates, a nonequilibrium microstructure is formed, containing metastable or incompletely transformed phases that are not reflected in equilibrium predictions. The XRD analysis in Bragg–Brentano mode is limited in detecting low volume fraction phases, especially those segregated in interdendritic regions. Moreover, peak overlapping between intermetallics and the BCC matrix hinders the precise resolution of complex phases such as Cu_4Ti_3 and $CuTi_2$. EDS analysis, in turn, provides only localized compositional resolution and is limited in distinguishing phases with similar compositions.

2.3. Mechanical Behavior and its Correlation with Microstructure

The morphology and porosity of the Cu_xMoNbTi alloys as a function of their Cu content are shown in **Figure 6**a,b, respectively.

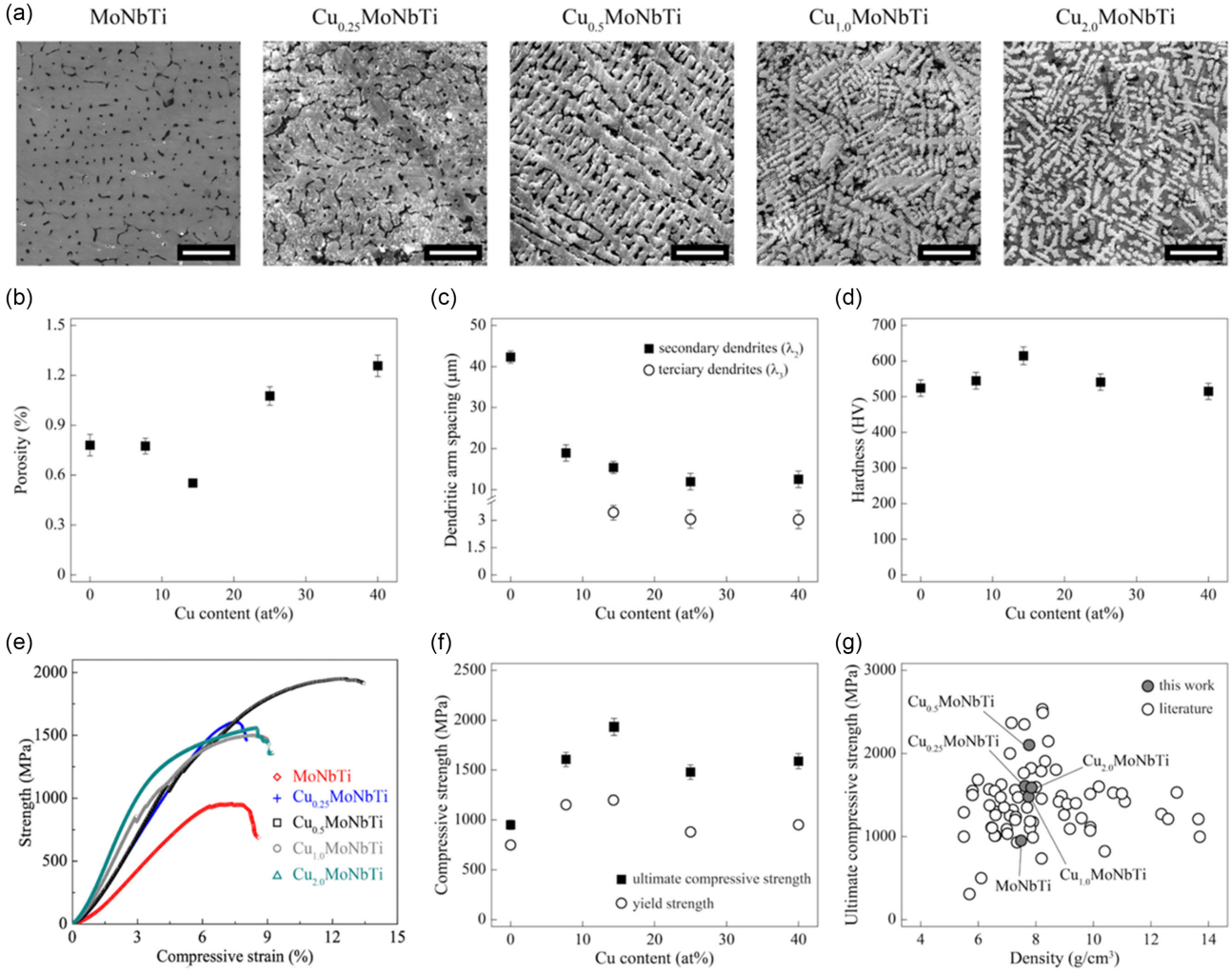

Figure 6. a) Morphology, b) porosity, c) secondary and tertiary dendrite arm spacings (λ_2, λ_3), and d) microhardness as a function of the Cu content in as-cast Cu_xMoNbTi alloys. e) Experimental stress–strain curves. f) Ultimate compressive strength and yield strength as a function of Cu content obtained from (e). g) Ultimate compressive strength and density of Cu_xMoNbTi alloys compared to other MPEAs.[16,31–43,56] Cu_xMoNbTi alloys with $x = 0$, 0.25, 0.5, 1.0, and 2.0 correspond to Cu contents of 0, 7.7, 14.3, 25, and 40 at%, respectively. Detailed Mechanical Data see Table S1, Supporting Information.

The lowest porosity value of $0.95 \pm 0.05\%$ was obtained for the $Cu_{0.5}$MoNbTi samples, while samples of different compositions displayed porosity values up to three times higher.

Figure 6c summarizes the variation in secondary (λ_2) and tertiary (λ_3) arm spacings with Cu content based on the SEM images in Figure 4. The addition of Cu leads to a substantial refinement of the microstructure, resulting in a more homogeneous distribution of CuTi-rich intermetallic phases. This refinement can be attributed to solute rejection and segregation during solidification. Although vacuum arc melting typically induces rapid cooling, which aids in microstructural refinement, the comparable cooling rates across the examined alloys suggest that Cu content is the primary factor driving these changes. As Cu segregates during solidification, it promotes the formation of dendritic structures associated with CuTi-rich intermetallic phases, particularly influencing their precipitation and distribution while reducing the fraction of the MoNb-rich phase (Figure 3).

Microhardness results, shown in Figure 6d, reveal that the addition of Cu increases hardness, peaking at 614 ± 48 HV for the $Cu_{0.5}$MoNbTi alloy. This improvement is attributed to solid solution hardening and the formation of hard intermetallic phases, both of which are influenced by Cu's effect on the crystalline structure and phase distribution. However, further Cu addition reduces hardness to 515 ± 25 HV for the Cu_2MoNbTi alloy, likely due to excessive formation of ductile Cu-rich phases, which changes the distribution of strengthening phases.

Compressive tests were conducted to characterize the Cu_xMoNbTi alloys. The stress-strain curves in Figure 6e confirm the superior mechanical properties of the $Cu_{0.5}$MoNbTi composition. Overall, the Cu-containing compositions exhibit ultimate compressive strength (UCS) values at least 1,5x higher than that of the MoNbTi alloy. The $Cu_{0.5}$MoNbTi alloy achieves the highest UCS, increasing by ≈2x (≈2000 ± 80 MPa) compared to MoNbTi (≈950 ± 50 MPa). The UCS and yield strength (YS) of the as-cast alloys are summarized in Figure 6f. Initially, the UCS and YS increase with Cu addition, peaking at $Cu_{0.5}$MoNbTi, before declining at higher Cu contents.

Compressive strain (ε_c) also reaches its maximum for the $Cu_{0.5}$MoNbTi alloy, with a value of ≈14%, representing a twofold increase compared to the reference alloy. This enhanced plasticity in compression is attributed to a uniform distribution of precipitates, which minimizes stress concentration and delays crack initiation. In contrast, alloys with less homogeneous precipitate distribution or higher fractions of brittle intermetallics exhibit limit plastic deformation, maintaining an unchanged ε_c.

The room-temperature UCS and density of Cu_xMoNbTi alloys were compared to those of other MPEAs in Figure 6g. While direct comparisons are challenging due to compositional differences, our Cu-containing alloys exhibit UCS values comparable to those of MPEAs containing structural and refractory metals, despite Cu being inherently softer and more ductile.[16,31–43] The mechanical properties of $Cu_{0.5}$MoNbTi can be attributed to the combined effects of reduced density, solid solution strengthening, and second-phase strengthening. Solidification conditions, influenced by alloy composition, cooling rates, and thermal gradients, play a crucial role in determining the dendritic microstructure and, consequently, the resulting mechanical performance.[28] Upon unchanged solidification conditions, our results indicate that Cu content is critical in tailoring the microstructure of Cu_xMoNbTi alloys. In the optimal alloy, $Cu_{0.5}$MoNbTi, a balance is achieved between the CuTi-rich phases, notably Cu_4Ti_3, and the MoNb-rich phase, which together create a fine and homogeneous dendritic structure ($\lambda_2 = 15.41$ μm) with well-anchored tertiary branches (Figure 3). This microstructure enhances hardness and

Table 2. Summary of the porosity, ultimate compressive strength (UCS), and morphology obtained for Cu_xMoNbTi alloys ($x = 0$, 0.25, 0.5, 1.0, and 2.0).

Cu content [at%]	Porosity [%]	UCS [MPa]	Morphology	Schematic representation
0	3 (±0.15)	950 (±50)	Equiaxed grains	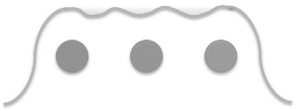
7.7	2.1 (±0.11)	1605 (±70)	Coarse dendritic arms	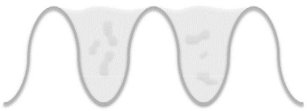
14.3	0.95 (±0.05)	2000 (±80)	Fine secondary and tertiary dendritic arms	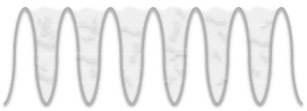
25	2.5 (±0.13)	1510 (±75)	Fine secondary and tertiary dendritic arms	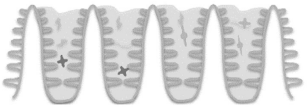
40	3.1 (±0.15)	1570 (±80)	Fine secondary and tertiary dendritic arms + Rosette-like CuTi-rich intermetallics	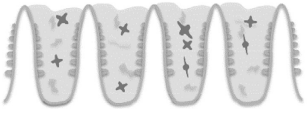

mechanical performance by distributing Cu–Ti phases effectively in the interdendritic regions, which reinforces the more ductile MoNb matrix and inhibits crack propagation. Conversely, the Cu_2MoNbTi alloy, despite having the finest dendritic spacing ($\lambda_2 = 11.95$ μm), contains an excessive volume of Cu-rich intermetallics, such as Cu_4Ti enveloped by Cu_4Ti_3, which compromises mechanical performance. The MoNbTi alloy ($x = 0$), by contrast, shows a coarser dendritic structure with poorly segregated particles and a higher volume fraction of the MoNb phase, leading to reduced mechanical performance. The differences in porosity, UCS, and morphology of Cu_xMoNbTi alloys are summarized in **Table 2** as a function of Cu content.

Several recent studies support these trends by highlighting the complex role of copper in HEAs and MPEAs. Verma et al.[22] and Zhang et al.[44] reported that Cu addition promotes interdendritic segregation and the formation of Cu-rich phases, which reduce toughness and increase brittleness in cast alloys. This is consistent with our observation of Cu–Ti intermetallics (e.g., Cu_4Ti_3, $CuTi_2$) forming in interdendritic regions at higher Cu contents. Chen et al.[45] and Babu et al.[46] showed that increasing Cu initially improves strength through phase stabilization but leads to softening when coarse FCC Cu-enriched phases form. Our results also reflect this behavior: $Cu_{0.5}$MoNbTi exhibits the best strength–ductility balance, while higher Cu contents result in performance loss. Hassan et al.[47] found that small Cu additions can enhance compressive strength if intermetallic distribution is fine and homogeneous, which helps explain the intermediate performance of $Cu_{0.25}$MoNbTi in our dataset. Xian et al.[21] and Yu et al.[18] emphasized that arc melting enhances Cu segregation in BCC matrices due to poor mutual solubility, as confirmed by our Scheil-based simulations. Yuan et al.[48] added that Cu can reduce dislocation density and recrystallize grains, contributing to lower yield strength at higher contents. Finally, Mosinoiu et al.[49] and Bablilas et al.[50] noted that Cu segregation can degrade mechanical integrity despite potential tribological or antibacterial benefits. These comparisons reinforce that Cu plays a dual role: improving microstructural refinement and strength at moderate contents but causing segregation-induced softening and brittleness at higher levels.

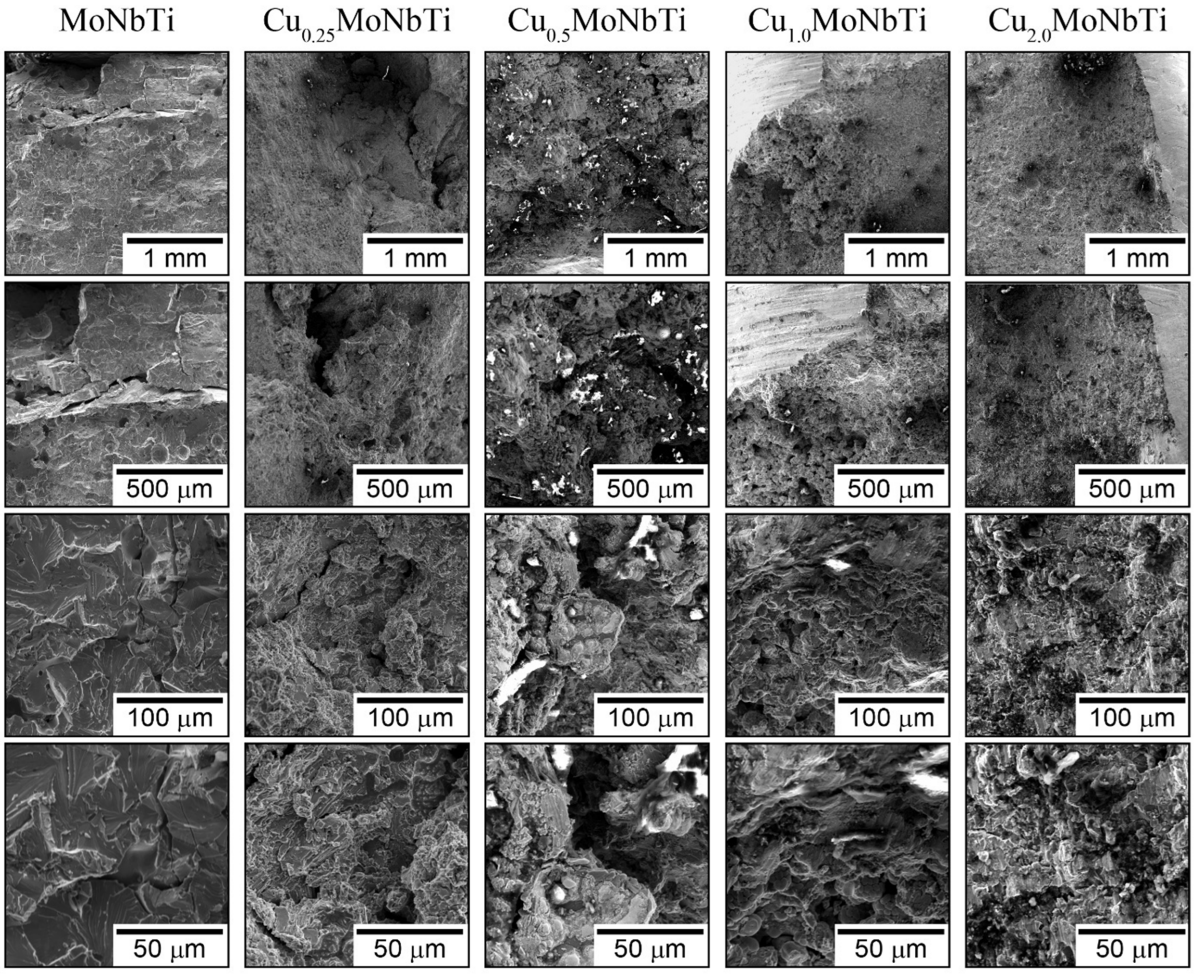

Figure 7. Fractographic SEM images of the Cu_xMoNbTi alloys after compression testing at different magnifications. The base MoNbTi alloy exhibits predominantly transgranular fracture with cleavage steps, while the $Cu_{0.25}$MoNbTi and $Cu_{0.5}$MoNbTi samples exhibit mixed-mode fracture surfaces with ductile dimples and evidence of intermetallic phase decohesion. $Cu_{1.0}$MoNbTi and $Cu_{2.0}$MoNbTi display increased porosity, brittle fracture features, and crack propagation along Cu-rich interdendritic regions, confirming the embrittling effect of excessive copper segregation.

Fractographic analysis (**Figure 7**) shows that fracture mechanisms vary within the Cu_xMoNbTi alloy series, in correlation with Cu content and mechanical performance. The Cu-free alloy (MoNbTi) exhibits a predominantly brittle fracture surface, characterized by cleavage planes and faceted features, indicating limited plastic deformation during crack propagation. With the progressive addition of Cu, a transition in fracture behavior occurs. $Cu_{0.25}$MoNbTi alloy shows mixed mode features, with cleavage steps and emerging dimples indicating some stress relaxation. $Cu_{0.5}$MoNbTi alloy exhibits well-defined dimples indicative of void nucleation, growth, and coalescence, signaling a transition to ductile fracture. This composition also exhibited uniform distribution of Cu without interfacial decohesion, contributing to improved strength and toughness. Conversely, alloys with higher Cu contents ($Cu_{1.0}$MoNbTi and $Cu_{2.0}$MoNbTi) display increased porosity and signs of interfacial debonding, along with brittle fracture features. Excessive segregation of Cu-rich phases and reduced matrix coherence in these samples likely undermine their mechanical integrity.

The results show that an intermediate Cu content ($Cu_{0.5}$MoNbTi) provides an optimal balance between plasticity and structural cohesion, enhancing both strength and fracture resistance. Xian et al.[21] noted that Cu's positive mixing enthalpy with elements such as Fe, Cr, Ni, Ti, and Co drives segregation during solidification. This Cu segregation forms weak interfaces that facilitate ductility loss and embrittlement, as also observed by Verma et al.[22] and Yu et al.[18]. Da Silva et al.[51] directly linked Cu segregation at grain boundaries to embrittlement and crack initiation.

Meng et al.[52] also reported that Cu-rich phases can reduce hardness and lower strength by increasing the fraction of ductile Cu-rich (FCC2) phases. Deformation mechanisms are also affected by increasing Cu levels. In the FeMnCoCr system studied by Yuan et al.,[48] higher Cu content stabilizes the austenite phase and raises the stacking fault energy. The dominant deformation mechanism shifts from martensitic transformation to a combination of transformation and mechanical twinning. Regarding fracture behavior, Miao et al.[53] indicated that increasing Cu content may enhance toughness, as evidenced by the growth of toughness-enhancing regions. However, the presence of Cu segregation may still facilitate crack nucleation and propagation along these interfaces.

Overall, high Cu content promotes segregation to weak interdendritic and interfacial zones, which compromises ductility and increases susceptibility to brittle fracture. By optimizing Cu content and refining the microstructure, a balance between hardness, strength, and plasticity in compression can be achieved, making these alloys promising candidates for applications requiring exceptional wear resistance and mechanical performance in extreme environments. These results highlight the significance of optimizing Cu content and controlling solidification parameters to achieve the desired phase balance and maximize mechanical properties.

3. Conclusion

This work investigates the effects of Cu content on the microstructural and mechanical properties of refractory Cu_xMoNbTi alloys. The results demonstrate that Cu plays a crucial role in tailoring dendritic morphology, phase evolution, and mechanical performance. 1) Microstructural Evolution: Phase diagram simulations and experimental characterization confirm that increasing Cu content refines the dendritic microstructure and promotes the formation of Cu–Ti intermetallic phases, including Cu_4Ti_3, Cu_3Ti_2, and CuTi. Higher Cu content shifts the phase equilibrium toward Cu-rich intermetallics while reducing the fraction of the MoNb-rich solid solution. The refinement of secondary (λ_2) and tertiary (λ_3) dendrite arm spacings increases with Cu content, resulting in a uniformly distributed interdendritic network. However, excessive intermetallic formation reduces the system's mixing entropy, potentially compromising thermal stability and increasing brittleness. This refinement can be attributed to solute rejection and segregation during solidification. 2) Densification and Porosity: The alloys exhibit high densification levels, ranging from 96% to 99%, with $Cu_{0.5}$MoNbTi achieving the lowest porosity ($0.95 \pm 0.05\%$). In contrast, excessive Cu addition leads to increased porosity, indicating a limit to its beneficial effects on microstructural refinement. 3) Hardness and Strength: Hardness increases with Cu addition, peaking at 614 ± 48 HV for $Cu_{0.5}$MoNbTi, before decreasing for Cu_2MoNbTi due to excessive formation of ductile Cu-rich phases. Similarly, ultimate compressive strength (UCS) peaks at $\approx 2000 \pm 80$ MPa for $Cu_{0.5}$MoNbTi, ≈2x increase compared to MoNbTi. The subsequent decline at higher Cu concentrations correlates with a shift in phase balance favoring softer Cu-rich intermetallics. This trend highlights Cu's dual role: precipitation hardening enhances strength at moderate concentrations, but excessive intermetallic formation reduces mechanical stability. 4) Plasticity in Compression: $Cu_{0.5}$MoNbTi exhibits the highest compressive strain ($\varepsilon_c \approx 14\%$), ≈1,7x that of MoNbTi. The formation of Cu–Ti intermetallics with Cu addition enhances plastic deformation by reducing stress concentrations and delaying crack initiation. However, alloys with excessive Cu content show reduced ε_c due to an increased fraction of brittle intermetallics. 5) Comparisons to Other MPEAs: The Cu_xMoNbTi alloys exhibit UCS values comparable to those of MPEAs composed of structural and refractory metals, with $Cu_{0.5}$MoNbTi reaching ≈2000 MPa. The interplay between solid solution strengthening, second-phase strengthening, and density reduction contributes to their mechanical properties.

Precise control of Cu content is essential to achieving an optimal combination of strength, hardness, and plasticity in compression. $Cu_{0.5}$MoNbTi emerges as the most promising composition, offering a refined microstructure that enhances mechanical performance. This study contributes to the broader understanding of phase evolution and mechanical optimization in MPEAs, supporting their potential for structural applications requiring high strength, wear resistance, and performance in extreme environments.

4. Experimental Section

Cu_xMoNbTi ($x = 0$, 0.25, 0.5, 1.0, and 2.0) MPEA ingots were manufactured by arc melting in an inert gas atmosphere. High-purity elemental Mo (99.9%, Sigma–Aldrich), Nb (99.8%, Sigma–Aldrich), Ti (99.7%, Sigma–Aldrich), and Cu (99.99%, Sigma–Aldrich) were used as starting materials for the alloy preparation. The samples were turned over and

remelted at least six times to achieve improved homogeneity. The crystal structures of the primary phases were examined using a Panalytical X'Pert powder diffractometer (Panalytical diffractometer, X'Pert model, Malvern, UK) using the Bragg-Brentano geometry at room temperature. The analysis was conducted with a Ni filter and Cu-Kα radiation, which had a wavelength of 0.15406 nm. The diffractometer was operated at a voltage of 45 kV and a current of 40 mA. The observed 2θ angle range spanned from 10° to 90°, with a step time of 10 s and an angular step of 0.008°. The patterns used for phase identification were acquired from the Pearson's Crystal Data program database.[54]

The microstructure of the MPEA ingots was characterized using scanning electron microscopy (SEM) (VEGA3, TESCAN, Brno, Czech Republic) and EDS, (XFlash 630M, Bruker, Billerica, USA). The SEM was operated with a tungsten filament at 20 kV and equipped with a four-quadrant backscattered electron detector (Type 400, Cambridge Scientific, Cambridge, USA). The backscattered electron detector used a 15 kV electron beam with a current of 2.82 nA, and a probe current of 1500 nA. The EDS detector, which had a resolution of 129 eV over a 30 mm^2 area, was operated with a 20 keV electron beam, a 15 mm focal length, and a current of 116 mA, resulting in a pulse throughput of 60 kcps.

Vickers microhardness measurements (Buehler, Wilson VH1102, Lake Bluff, USA) were performed in accordance with the ASTM T1 standard. The polished surfaces of the samples were probed at least 10 times each with an external force of 2.9 N exerted for 15 s. Compressive tests of the alloys were conducted using a universal electro-hydraulic servo machine at room temperature with a loading speed of 25 mm min^{-1} and a strain rate of 2×10^{-4} s^{-1}. To ensure reproducibility, average values were calculated from triplicate tests. For these measurements, cylindrical specimens with a diameter of 6 (±0.08) mm and a height of 12 (±0.05) mm were used. The yield strength was calculated by considering a strain shift of 0.2% from the elastic zone.

The equilibrium phase diagrams were calculated with specialized software (Thermo-Calc, version 2023b, Råsundavägen 18 SE-169 67 Solna SWEDEN, Sweden) and the TCHEA6 (HEAs version 6.1) database.[55]

Supporting Information

Supporting Information is available from the Wiley Online Library or from the author.

Acknowledgements

The authors would like to thank the financial support from CAPES, CNPq through the research grant no. 305207/2023-7, FAPESP under grant nos. 2016/13352-0 and 2013/12729-5, and FAEPEX for funding project no. 3511/24. The authors also thank the technical support provided by the institutions involved in the development of this work.

The Article Processing Charge for the publication of this research was funded by the Coordenação de Aperfeiçoamento de Pessoal de Nível Superior - Brasil (CAPES) (ROR identifier: 00x0ma614).

Conflict of Interest

The authors declare no conflict of interest.

Author Contributions

Eder Lopes Ortiz: methodology (equal). **João Felipe Queiroz Rodrigues**: data curation (equal); methodology (equal). **Renato Baldan**: investigation simulation by CalPHAD (equal); writing—original draft (supporting). **Erik Poloni**: data curation (supporting); investigation (supporting); writing—original draft (equal). **Giovana da Silva Padilha**: data curation (supporting); methodology (supporting); writing—original draft (supporting). **Wislei Riuper Osório**: data curation (supporting); formal analysis (supporting); investigation (supporting); writing—original draft (supporting). **Ausdinir Danilo Bortolozo**: conceptualization (lead); formal analysis (equal); investigation (equal); methodology (supporting); supervision (lead); writing—original draft (lead).

Data Availability Statement

The data that support the findings of this study are available from the corresponding author upon reasonable request.

Keywords

copper, mechanical properties, microstructure, multiprincipal elements alloys

Received: March 28, 2025
Revised: July 31, 2025
Published online: September 2, 2025

[1] S. K. Dewangan, A. Mangish, S. Kumar, A. Sharma, B. Ahn, V. Kumar, *Eng. Sci. Technol. Int. J.* **2022**, *35*, 101211.
[2] W. Li, D. Xie, D. Li, Y. Zhang, Y. Gao, P. K. Liaw, *Progr. Mater. Sci.* **2021**, *118*, 100777.
[3] T. Sonar, M. Ivanov, E. Trofimov, A. Tingaev, I. Suleymanova, *Mater. Sci. Energy Technol.* **2024**, *7*, 35.
[4] B. Cantor, *Progr. Mater. Sci.* **2021**, *120*, 100754.
[5] W. Steurer, *Mater. Charact.* **2020**, *162*, 110179.
[6] P. Sharma, V. K. Dwivedi, S. P. Dwivedi, *Mater. Today: Proc.* **2021**, *43*, 502.
[7] Y. A. Alshataif, S. Sivasankaran, F. A. Al-Mufadi, A. S. Alaboodi, H. R. Ammar, *Metals Mater. Int.* **2020**, *26*, 1099.
[8] J.-X. Hou, B.-X. Cao, B. Xiao, Z.-B. Jiao, T. Yang, *Rare Metals* **2022**, *41*, 2002.
[9] H. Zheng, L. T. W. Fey, X.-G. Li, Y.-J. Hu, L. Qi, C. Chen, S. Xu, I. J. Beyerlein, S. P. Ong, *Comput. Mater.* **2023**, *9*, 89.
[10] L. H. de Almeida, I. N. Bastos, I. D. Santos, A. J. B. Dutra, C. A. Nunes, S. B. Gabriel, *J. Alloys Compd.* **2014**, *615*, S666.
[11] A. R. V. Nunes, S. Borborema, L. S. Araújo, T. Z. L. Rodrigues, L. Malet, J. Dille, L. H. de Almeida, *Metals* **2023**, *13*, 1889.
[12] H. Wang, F. Wang, H. Liu, D. Pan, Q. Pan, Y. Liu, J. Xiao, P. Zhang, *Mater. Sci. Eng.: A* **2016**, *667*, 326.
[13] H. Liu, R. Wang, Q. Gao, P. Chen, J. Hao, H. Yang, X. Liu, *Mater. Charact.* **2023**, *206*, 113449.
[14] Y. Chen, B. Li, *J. Phys.: Conf. Ser.* **2023**, *2419*, 012074.
[15] D. G. Kalali, A. Kanchi, P. S. Phani, K. B. S. Rao, S. V. S. N. Murty, K. V. Rajulapati, *Int. J. Refract. Metals Hard Mater.* **2024**, *118*, 106487.
[16] G. Cieślak, J. Dąbrowa, M. Jawańska, A. Parzuchowska, D. Oleszak, *Metall. Mater. Trans. A* **2022**, *53*, 653.
[17] P. Agrawal, S. Gupta, S. Shukla, S. S. Nene, S. Thapliyal, M. P. Toll, R. S. Mishra, *Mater. Design* **2022**, *215*, 110487.
[18] Y. Yu, N. Xu, S. Zhu, Z. Qiao, J. Zhang, J. Yang, W. Liu, *J. Mater. Sci. Technol.* **2021**, *69*, 48.
[19] J. Dąbrowa, G. Cieślak, M. Stygar, K. Mroczka, K. Berent, T. Kulik, M. Danielewski, *Intermetallics* **2017**, *84*, 52.
[20] Q. C. Fan, B. S. Li, Y. Zhang, *J. Alloys Compd.* **2014**, *614*, 203.
[21] X. Xian, L. Lin, Z. Zhong, C. Zhang, C. Chen, K. Song, J. Cheng, Y. Wu, *Mater. Sci. and Eng.: A* **2018**, *713*, 134.
[22] A. Verma, P. Tarate, A. C. Abhyankar, M. R. Mohape, D. S. Gowtam, V. P. Deshmukh, T. Shanmugasundaram, *Scr. Mater.* **2019**, *161*, 28.

[23] J. Wang, H. Jiang, X. Chang, L. Zhang, H. Wang, L. Zhu, S. Qin, *Corros. Sci.* **2023**, *221*, 111313.
[24] W. Kurz, D. Fisher, and M. Rappaz, *Fundamentals of Solidification*, (**2023**).
[25] M. Gündüz, E. Çadırlı, *Mater. Sci. Eng.: A* **2002**, *327*, 167.
[26] Y. G. Li, H. Chen, Y. C. Huang, W. Y. Liu, *J. Mater. Eng. Perform.* **2024**, *33*, 11289.
[27] C. Aguilar, D. Guzman, P. A. Rojas, S. Ordoñez, R. Rios, *Mater. Chem. Phys.* **2011**, *128*, 539.
[28] F. Liu, Q. Song, R. Chen, C. Wang, J. Sun, *Vacuum* **2023**, *210*, 111830.
[29] M. J. Bermingham, S. D. McDonald, D. H. StJohn, M. S. Dargusch, *J. Mater. Res.* **2009**, *24*, 1529.
[30] T. B. Massalski, H. Okamoto, P. Subramanian, L. Kacprzak, W. W. Scott, *Alloy Phase Diagrams*, **2016**, https://doi.org/10.31399/asm.hb.v03.9781627081634.
[31] X. Gao, L. Wang, N. Guo, L. Luo, G. Zhu, C. Shi, Y. Su, J. Guo, *Int. J. Refract. Metals Hard Mater.* **2022**, *102*, 105723.
[32] H. Chen, A. Kauffmann, B. Gorr, D. Schliephake, C. Seemüller, J. N. Wagner, H.-J. Christ, M. Heilmaier, *J. Alloys Compd.* **2016**, *661*, 206.
[33] M. Zhang, X. Zhou, J. Li, *J. Mater. Eng. Perform.* **2017**, *26*, 3657.
[34] J. Yi, L. Wang, M. Xu, L. Yang, *Mater. Tehnol.* **2021**, *55*, 305.
[35] W. Zhang, W. Jiang, S. Wu, S. Tao, B. Zhu, S. Guo, *Adv. Eng. Mater.* **2022**, *24*, 6.
[36] A. Akinwekomi, F. Akhtar, *Materials* **2023**, *16*, 5320.
[37] D. Li, W. Li, X. Liu, *J. Alloys Compd.*, **2024**, https://doi.org/10.2139/ssrn.5065176.
[38] L. Li-Yan, C. Shu-nan, L. Yi, J. Gang, C. Hai-Dong, J. Yun-Jie, L. Chang-Jiu, L. Cheng-Xin, *Int. J. Refract. Metals Hard Mater.* **2022**, *104*, 105784.
[39] O. N. Senkov, G. B. Wilks, J. M. Scott, D. B. Miracle, *Intermetallics* **2011**, *19*, 698.
[40] O. N. Senkov, S. V. Senkova, C. Woodward, *Acta Mater.* **2014**, *68*, 214.
[41] W. Chen, Q. H. Tang, H. Wang, Y. C. Xie, X. H. Yan, P. Q. Dai, *Mater. Sci. Technol.* **2018**, *34*, 1309.
[42] R. Zhang, K. Tulugan, A. Zhang, J. Meng, J. Han, *J. Mater. Eng. Perform.* **2022**, *31*, 984.
[43] Z. Li, L. Wang, B. B. Wang, S. S. Li, Z. W. Li, L. S. Luo, R. R. Chen, Y. Q. Su, J. J. Guo, *Mater. Sci. Eng.: A* **2022**, *844*, 143072.
[44] X. Zhang, Y. Yu, T. Li, L. Wang, Z. Qiao, Z. Liu, W. Liu, *Tribol. Int.* **2024**, *193*, 109401.
[45] W. Chen, S. Liu, J. Jiang, W. He, B. Liang, J. Zhang, Y. Ai, *J. Mater. Eng. Perform.* **2025**, *34*, 2862.
[46] P. D. Babu, P. Dongre, A. Moganraj, N. A. Nambiraj, G. Manivasagam, J. Sure, *Mater. Today Commun.* **2024**, *40*, 109579.
[47] M. A. Hassan, H. M. Yehia, A. S. A. Mohamed, A. E. El-Nikhaily, O. A. Elkady, *Crystals* **2021**, *11*, 540.
[48] Y. Yuan, J. J. Wang, J. Wei, W. Y. Chen, H. L. Yan, N. Jia, *J. Alloys Compd.* **2024**, *970*, 172543.
[49] L. F. Mosinoiu, A. Sobetkii, B. A. Serban, L. M. Cursaru, A. C. Matei, M. Ghita, N. Vitan, S. Caramarin, D. Mitrica, A. Pogrebnjak, B. Postolnyi, *J. Mater. Res. Technol.* **2025**, *35*, 6261.
[50] R. Babilas, M. Kądziołka-Gaweł, A. Bajorek, P. Gębara, A. Radoń, T. Warski, O. Bialas, M. Spilka, W. Łoński, K. Młynarek-Żak, *Arch. Civil Mech. Eng.* **2024**, *25*, 48.
[51] A. Kwiatkowski da Silva, R. D. Kamachali, D. Ponge, B. Gault, J. Neugebauer, D. Raabe, *Acta Mater.* **2019**, *168*, 109.
[52] C. Meng, Z. Song, X. Qiu, G. Wang, C. Wu, X. Ren, W. Zhuang, X. Wang, *J. Alloys Compd.* **2023**, *934*, 167896.
[53] L. Miao, Y. Cao, J. Liu, Y. Xu, L. Sun, S. Zhou, *Vacuum* **2024**, *227*, 113369.
[54] P. Villars, K. Cenzual, *Pearson's Crystal Data: Crystal Structure Database for Inorganic Compounds*, ASM International, Materials Park, Ohio, USA.
[55] J.-O. Andersson, T. Helander, L. Höglund, P. Shi, B. Sundman, *Calphad* **2002**, *26*, 273.
[56] J.-P. Couzinié, O. N. Senkov, D. B. Miracle, G. Dirras, *Data Brief*, **2018**, *21*, 1622.